ACS APPLIED MATERIALS & INTERFACES

Research Article

Cite This: ACS Appl. Mater. Interfaces XXXX, XXX, XXX−XXX

www.acsami.org

Highly Switchable Adhesion of N-Doped Graphene Interfaces for Robust Micromanipulation

Yiyang Wan,[†,§] Yong Gao,[†,‡,§] and Zhenhai Xia*[,†,‡]

[†]Department of Materials Science and Engineering, and Department of Chemistry, University of North Texas, Denton, Texas 76203, United States

[‡]School of Materials Science and Engineering, Northwestern Polytechnical University, Xi'an, Shaanxi 710072, P. R. China

Supporting Information

ABSTRACT: We demonstrated an N-doped graphene interface with highly switchable adhesion and robust micromanipulation capability triggered by external electric signals. Upon applying a small dc or ac electrical bias, this nanotextured surface can collect environmental moisture to form a large number of water bridges between the graphene and target surface, which lead to a drastic change in adhesive force. Turning on and off the electrical bias can control this graphene interface as a robust micro/nanomanipulator to pick up and drop off various micro/nano-objects for precise assembling. Molecular dynamics simulation reveals that the electrically induced electric double layer and ordered icelike structures at the graphene−water interface strengthen the water bridges and consequently enhance force switchability. In addition to the micro-/nanomanipulation, this switchable adhesion may have many technical implications such as climbing robots, sensors, microfluidic devices, and advanced drug delivery.

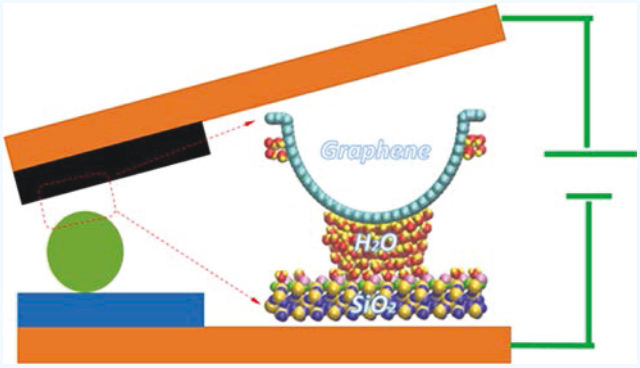

KEYWORDS: *switchable adhesion, manipulation, electric modulation, graphene, molecular dynamics simulation*

1. INTRODUCTION

Smart surfaces or interfaces, which can turn their adhesive force on and off spontaneously under natural or provoked stimuli, renders them appealing for many applications such as climbing robots, transport systems, micromanipulators, sensors, microfluidic devices, advanced drugdelivery, and so forth.[1−4] Over the past decade, a variety of approaches have been pursued to create switchable adhesion triggered by various stimuli, including temperature change that induces phase transitions in polymers,[5,6] light emission that results in cross-linking of light-sensitive polymers,[7] pH change that alters the shape of electrically charged polymers,[8] solvent concentration in polymer brush systems,[9] magnetic fields,[10] and mechanical force in a wrinkled material system.[11] These switchable surfaces, however, are made mostly from stimuli-responsive materials (e.g., piezoelectric and electrostrictive) by self-assembling or grafting functional molecules.[12,13] Although these surfaces have several advantages, including fast responsivity and good switchability, they also suffer from instability, short lifetime, and fouling. Few materials could achieve a robust switchable interface for frequent contacting.

In nature, many insects and animals use quite different strategies to alter the adhesion of their attachment systems for locomotion and predation.[14,15] For example, gecko feet can rapidly switch on and off their dry adhesive force to run on vertical walls and ceilings.[14] Mimicking the gecko-foot hair arrays, the artificial gecko foot hairy arrays made of micro- or nanofibers have been developed, which show controllable adhesive forces by adjusting detaching directions or retreating speeds.[16,17] Capillarity-based switchable adhesion was created by imitating the bristle pads of palmetto beetles that can form a large number of parallel micron-sized liquid bridges between their feet and substrates.[15] In this capillary adhesion device, liquid was pumped through a number of small holes with spacers to form a number of liquid bridges between the device and the substrate to create strong adhesion.[18]

In this work, we demonstrated an N-doped graphene surface, a nonstimuli-responsive material that showed highly switchable adhesion modulated by electric signals. Instead of pumping water to the interface from a water reservoir, water vapor was harvested from the air or surroundings to generate water bridges between the graphene and substrate. The surface can pick up, transform, and drop down various microparticles and microfibers for precise patterning without grabbing the objects by force. The adhesion-switchable mechanism was revealed by molecular dynamics (MD) simulations.

Received: October 26, 2018
Accepted: January 16, 2019
Published: January 16, 2019

DOI: 10.1021/acsami.8b18793
ACS Appl. Mater. Interfaces XXXX, XXX, XXX−XXX

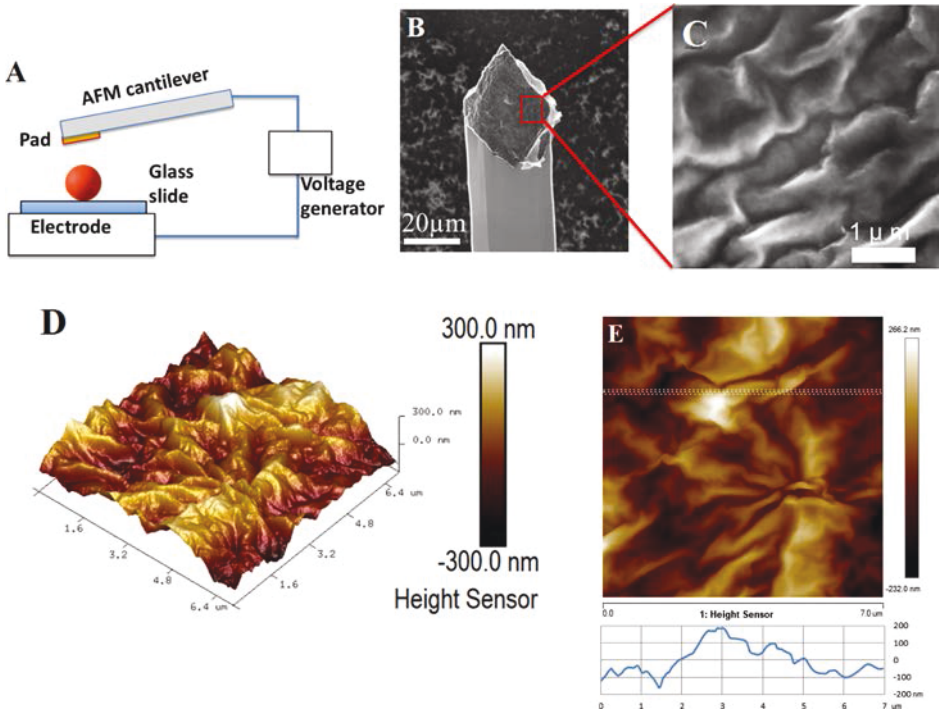

Figure 1. Graphene structure and its tunable adhesive force under external electrical bias. (A) Schematic of experimental setup in AFM. SEM images of (B) AFM cantilever glued with the graphene micropad, used for adhesion measurement, and (C) graphene on the surface with nanoscale concave-convex texture. (D) 3D AFM image of N-doped graphene, scanned in the contact mode in RH 30% and room temperature, with a scanning size of 7 μm. (E) 2D AFM image of N-doped graphene with step configuration along the dotted line.

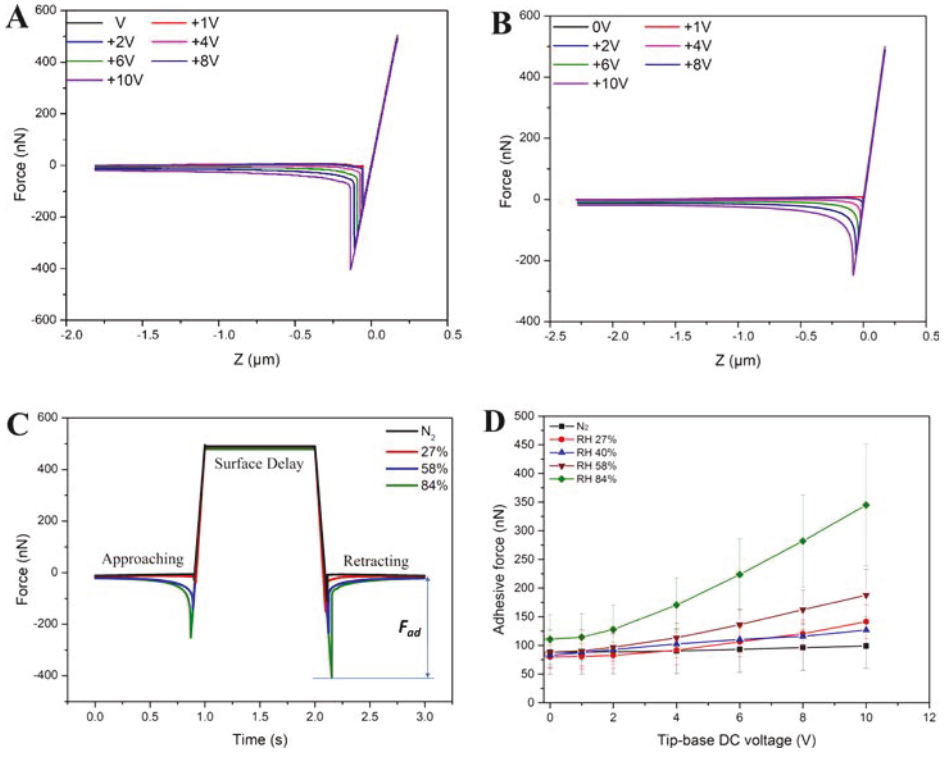

Figure 2. Force−distance curves for adhesion measurement and tunable adhesive force under external electrical bias. (A) Typical retracting force−distance curves measured for N-doped graphene materials on SiO_2 microspheres under different applied biases at 84% RH. (B) Approaching force−distance curves measured for N-doped graphene materials on SiO_2 microspheres under different applied biases at 84% RH. (C) Force−time curves measured for N-doped graphene materials on SiO_2 microspheres at +10 V biases in different RHs. (D) Adhesive forces between the graphene pad and SiO_2 microspheres as a function of dc bias at different RHs. The adhesive force F_{ad} is defined in (C).

DOI: 10.1021/acsami.8b18793
ACS Appl. Mater. Interfaces XXXX, XXX, XXX−XXX

2. RESULTS

2.1. Nanostructures with Electrically Induced Switchable Adhesion. N-doped graphene flakes were synthesized with the chemical vapor deposition method, and the process was reported in detail elsewhere.[19] Selected N-doped graphene flakes (~5 layers, ~30 μm in size) were picked up and glued on an atomic force microscope (AFM) tipless probe for adhesion testing in an AFM system (Figure 1A,B). The details of the fabrication process for the graphene AFM tips are described in the Methods section. Graphene has been reported to have the ability to generate ultra-strong adhesion over various surfaces.[20] After it is doped with nitrogen, the graphene becomes wrinkled naturally, with nanoscale concave−convex textures on its surface (Figure 1C,D). These nanotextured graphene surfaces significantly increase surface compliance.[15] In addition, this nanoconvex structure promotes local adsorption becaue of the tip effect under applied electric potential.[21,22]

Using AFM, we examined the adhesion of the textured graphene surface on a variety of spherical microparticles in customized chamber environments under different applied electric potentials. dc potential was applied between the AFM tip and substrate electrode, as schematically shown in Figure 1A. The graphene pad on the AFM tip was engaged, made a contact (~5 s) with a microsphere (~10 μm in diameter) fixed on a glass slide (1 mm in thickness), and retreated from the microsphere surface. The typical retracting/approaching force−displacement and force−time curves were recorded and shown in Figure 2A−C, respectively. The attractive forces acting on the tip in the approach curve in Figure 2B is much larger than expected for a macroscopic distance (slide thickness). Similarly, the force also remains high after the snap during retreating. It seems there were strong electrostatic interactions between the graphene pad and the microsphere surface. The adhesive force F_{ad} is defined as the maximum retracting force relative to the base line (with no bias), as schematically illustrated in Figure 2C.

Figure 2D shows the adhesive force as a function of the applied bias, measured at a relative humidity (RH) from 0 to 90%. For the measurement at 0% RH, the graphene pads were kept in the chamber filled with dry N_2 for 24 h and then tested using the same procedure. In the dry N_2 environment (0% RH), the applied voltage has almost no effect on the adhesive force (Figure 2C,D). As the humidity increases, the adhesive force becomes dependent of voltage change, and it increases rapidly with increasing the applied bias. Thus, the presence of water plays a critical role in modulating the adhesive force by electrical bias.

For comparison, three more materials, low-density polyethylene (LDPE), aluminum (Al), and Teflon thin films were carefully selected according to their surface properties (Table 1). Among these selected materials, Teflon is superhydrophobic while LDPE is hydrophilic, but both are insulative. On contrary, Al is conductive similar to N-doped graphene, and the wetting angles of both materials are below but close to 90°. The adhesion measurements were performed with the same experimental procedure under the same environmental conditions. Figure 3A−C shows the adhesive forces of Al, Teflon, and LDPE thin films versus applied electric bias, respectively, and Figure 3D provides the comparison between these materials under the same applied electric bias and RH. Overall, for the insulative materials, the adhesive force is almost independent of the potential change, but for the conductive materials, it increases with increasing the applied electric potential. In particular, for the graphene, the adhesive force increased by ~6 times at 15 V in 84% RH.

Table 1. Measured Surface Wetting Properties of Pad Materials

pad material	wetting angle
N-doped graphene[23]	>85°
aluminum	86.9°
LDPE	55.9°
Teflon	133.7°

To test the response time of these material surfaces, the adhesive force was continuously measured by repeating the approach−contact−retraction cycles. At a high humidity (84% RH), the force almost immediately increased to its maximum value in response to the bias, but at a relatively low RH (58%), the force reached the same maximum value within 10 s after the potential was on (Figure 4A). Upon turning off the electric bias, the adhesive force returned to its normal values in 10 s. The adhesive force is independent of the contact time except for the very short contact time (<10 s) (Figure 4B). Interestingly, the adhesive force also responds to frequency under ac bias. The typical force−distance curves under ac bias are shown in Figure 5A. Under the ac bias, the force change induced by low ac frequency can still be clearly seen during retreating. As shown in Figure 5B, the graphene pad delivered higher adhesive force at lower frequency but much lower force at higher frequency. The adhesion also increased in response to higher ac voltage (Figure 5C). Other materials exhibited the similar response to the frequency, but only conductive materials responded more strongly to the frequency (Figure 5D). Among these materials tested in the experiment, the graphene stands out in switchability under ac biases as well.

2.2. Electrically Modulated Micromanipulators. The highly switchable graphene surface would enable a variety of applications such as micromanipulation, climbing robots, and microelectromechanical systems. As an example to show its switchable capability to manipulate microobjects in a non-grabbing way, we tested the N-doped graphene pad to pick up, transport, and drop off microparticles for precise micro/nanomanipulation and assembly. For conventional micromanipulators, it is usually a challenge to pick up microobjects because of low adhesion. Even if one manages to pick up the objects, it is not easy to drop off because of its unchangeable adhesive force. Using the graphene pad attached on an AFM probe as a micromanipulator, we successfully manipulated microspheres on glass substrates and were able to pick up, drop off, and precisely assemble the micro-sized objects (1−100 μm) in a patterned fashion, including SiO_2 and polystyrene microspheres (Figure 6A). The manipulation processes, including pick-up under an electric bias, and drop-off by turning off the electric signals, were demonstrated (Supporting Information, Movie S1). In addition to microspheres, the micromanipulator can also manipulate other types of small objects such as debris and microfiber segments. Figure 6B,C shows the probability of microsphere attachment events in a 30-trial experiment at dc and ac electric biases, respectively. The probability of particle attachment rapidly ramps up and reaches ~100% when the dc bias is increased to a value of 10 V. For detachment, lateral shearing is proved to effectively break water bridges. The microparticles adhering to the

DOI: 10.1021/acsami.8b18793
ACS Appl. Mater. Interfaces XXXX, XXX, XXX−XXX

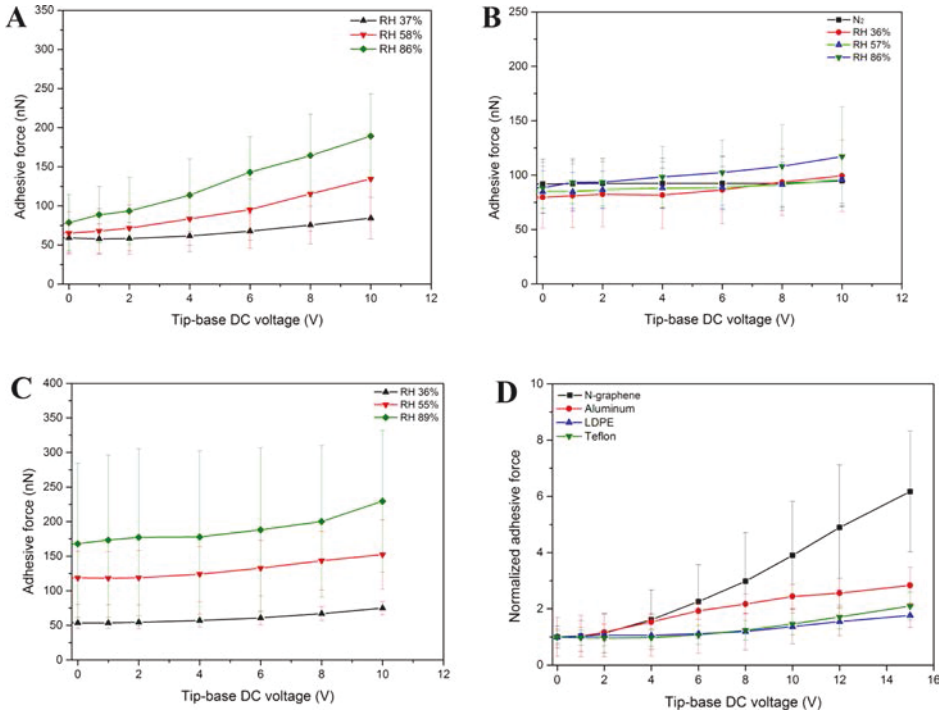

Figure 3. Adhesive force measured for the pads with different materials. Adhesive force as a function of applied voltage for (A) Al, (B) Teflon, and (C) LDPE pads at different RHs. (D) Adhesive forces on microparticles, normalized by that at zero voltage, for the graphene, Al, Teflon, and LDPE pads, as a function of dc bias at a RH of 84%. Engaging and retracting speeds are 2 μm/s, with a preload of 150 nN, 5 s contact time, and 0 shearing.

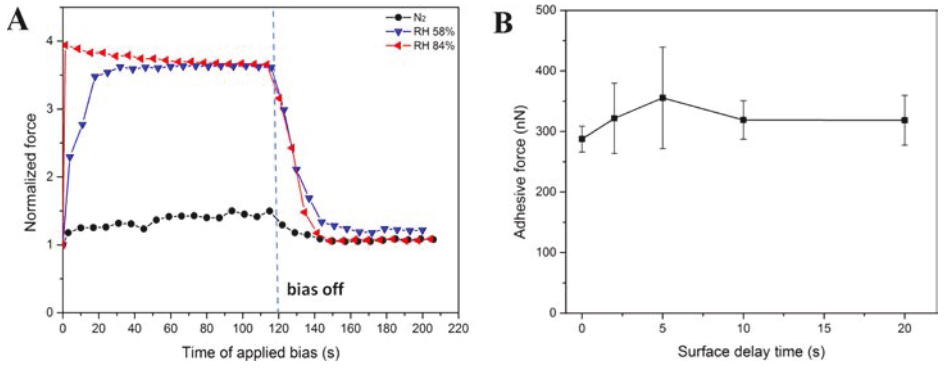

Figure 4. Adhesive forces, normalized by that at zero voltage, as a function of contacting time at an applied dc voltage of 10 V. (A) Adhesion force of the graphene pad on the SiO_2 microsphere as a function of time at different RHs, (B) effect of contact time on the adhesive forces of graphene pads at 86% RH with an engaging and retracting speeds of 2 μm/s and a preload of 150 nN.

graphene pad can be detached and dropped precisely to the desired positions by switching off the electric signal and applying a small shear sliding, mimicking the gecko feet movement.[15] Thus, this electrically switchable graphene micromanipulator is reliable and robust in manipulating various microobjects.

To examine the durability of the micromanipulator, we repeatedly made the attachment and detachment on SiO_2 microspheres (diameter $\approx$ 10 μm) at a frequency of 6 s per cycle and a preload of 150 nN under a tip bias of 10 V and found no abnormal even after 50 000 cycles (Figure 6D). Even if the pad was damaged, it could be repaired by gluing a new piece of graphene on the damaged pads. These results demonstrated that the graphene with switchable adhesion are robust and efficient in micromanipulation. All of these features of the graphene enable many practical applications related to controllable manipulation and immobilization of microparticles.

2.3. Molecular Dynamics Simulation of Switchable Adhesion. MD simulation was performed to understand the role of water and interfacial topology in switchable adhesion. Because peaks and valleys are the typical topological structure on the wrinkled graphene surface, a nanoscale convex graphene surface was chosen as a unit cell together with the SiO_2 substrate. Because the excess charges are all on the surface of a conductor, charges were uniformly distributed on the surface of the graphene. Silanol groups were grafted on the SiO_2 surface with certain density (13 groups/nm^2), and an electric double layer (EDL) was then formed with the silanol groups and water adsorption (Figure 7A).[24−26] Similar with the realistic SiO_2 surface in a humid environment, the substrate surface was covered with water in a certain thickness (0−1

DOI: 10.1021/acsami.8b18793
ACS Appl. Mater. Interfaces XXXX, XXX, XXX−XXX

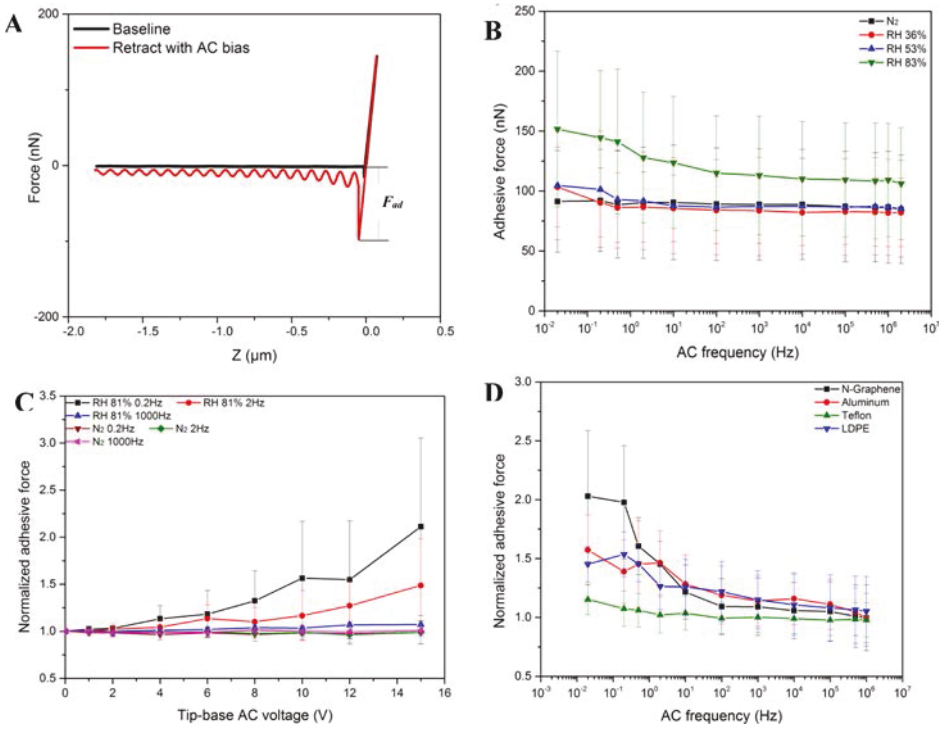

Figure 5. Adhesion forces measured at different frequencies of ac signals. (A) Force vs retreating distance under ac bias, on which the adhesive force F_{ad} is defined, (B) adhesive force of the graphene pad as functions of frequency and RH at a ac potential of 10 V, and (C) adhesive force of the graphene pad at different ac voltages, normalized by that at zero bias. (D) adhesive forces at an ac potential of 15 V for graphene, Al, LDPE, and Teflon pads, normalized by that at zero bias, as a function of frequency at 85% RH. Engaging and retracting speeds are 2 μm/s, with a preload of 150 nN and a contacting time of 5 s.

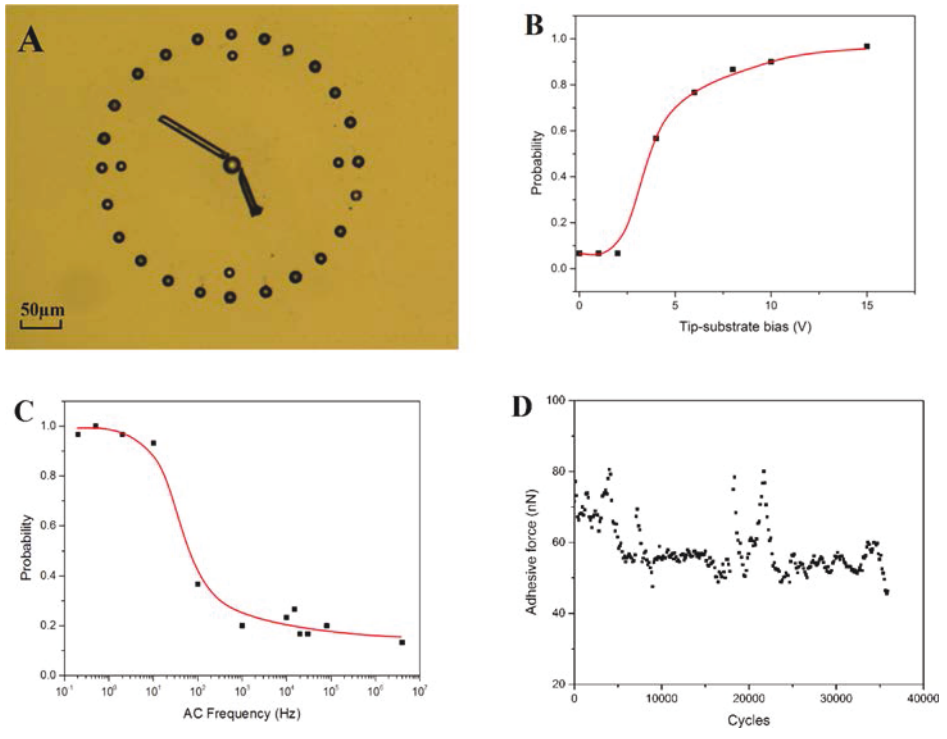

Figure 6. Micromanipulation of microparticles by bioinspired micromanipulators. (A) Photograph of the pattern made of microspheres and microfibers by using the biomimetic micromanipulator, (B) probability of particle pick-up with the graphene pad as a function of the applied voltage, (C) probability of particle pick-up with the graphene pad as function of frequency under an ac bias of 10 V, and (D) adhesive force as a function of cycles operated at 0.3 Hz under a tip bias of 10 V at ~50% RH. Note that the contact position was shifted at 18 000 cycles in the cyclic test, which causes abnormal peaks on the curve.

DOI: 10.1021/acsami.8b18793
ACS Appl. Mater. Interfaces XXXX, XXX, XXX−XXX

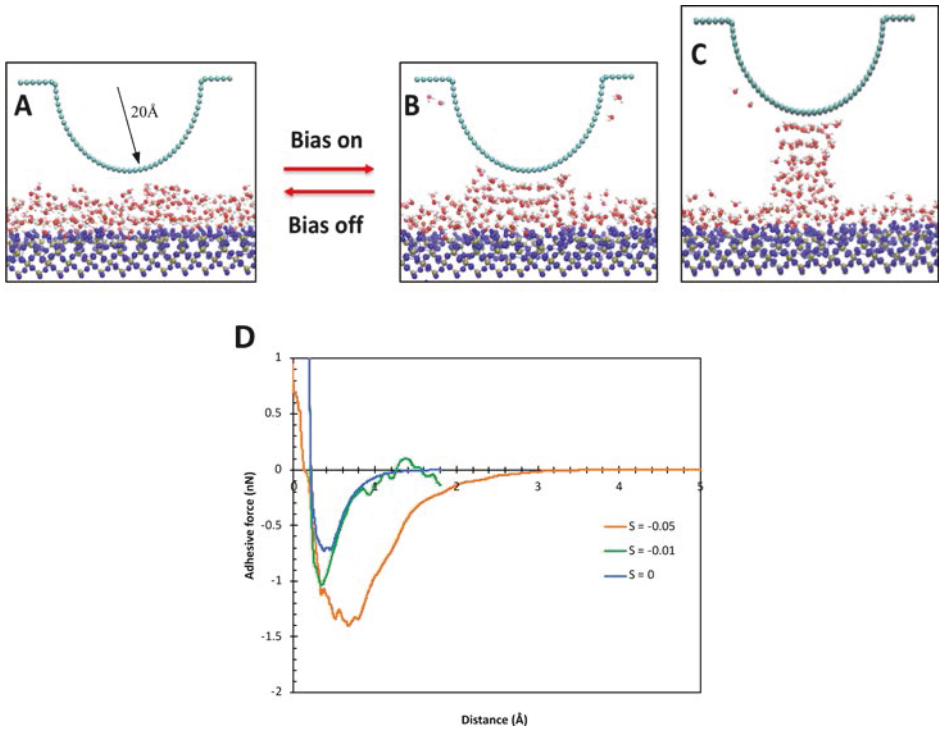

Figure 7. MD simulation of the tunable adhesive force under external electrical bias. Water molecular structures near a convex graphene layer (A) without applied electric bias, (B,C) under an electric bias, simulated using MD methods. White and red balls represent hydrogen and oxygen in water; cyan balls represent carbon in graphene; and yellow, blue, and tan balls refer to silicon, oxygen, and hydrogen atoms in silicon oxide, respectively. (D) Predicted adhesive force on the SiO_2 substrate covered with a 0.5 nm water layer against the retreating distance for different applied electric charge density S (unit charge/atom).

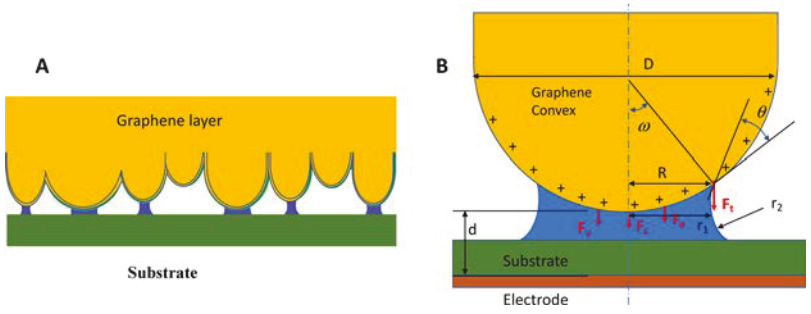

Figure 8. Schematic illustrations of graphene pads contacting the target surface and water bridge. (A) Water bridges formed between the nanoconvex regions and target surface upon applying electric bias. (B) Geometry of the water bridge envelope (meniscus) between the graphene layer and the surface.

nm) depending on the humidity.[25] Following the experimental procedure of the adhesive force measurement, the graphene convex layer was made to contact with the substrate and the adhesive force was calculated. Figure 7 shows the water bridge structures and the calculated adhesive force (F_{ad}) versus separation distance r for the substrate with ~0.5 nm of the water layer and different electric biases (charge density S). In the case of no applied bias, small water bridges were observed at the graphene interface because of the nonwetting nature of the graphene surface (wetting angle > 85°, Table 1), but with the bias applied on the system, large water bridges are formed during the retraction (Figure 7B,C). The simulated force–separation curves (Figure 7D) are consistent with the experimental results that in the presence of water, the adhesive force increases with increasing the electric bias. In the bridges, water molecules are aligned to form an icelike structure, indicating that the applied bias facilitates the electrical wetting on the convex surface and thus enhances the adhesion force.

3. DISCUSSION

The unusual strong force modulation of the graphene surface is attributed to its high conductivity, excellent flexibility, unique surface microstructures, and ability to collect water from the surroundings. As aforementioned, the graphene has a nano-textured surface; its roughness R_a and R_q, measured by AFM, are 63.3 and 77.0 nm, respectively, with a maximum peak-valley depth of ~300 nm (Figure 1D,E). There are a large number of peaks or nano-convex regions on the flexible surface of the graphene. In the adhesion test, these nano-convex regions would contact with the target surface to form water bridges, as schematically illustrated in Figure 8. Although water bridges can be formed between the AFM tip and substrates without electrical bias,[27] the adhesion between the surface and

DOI: 10.1021/acsami.8b18793
ACS Appl. Mater. Interfaces XXXX, XXX, XXX−XXX

water bridge decreases rapidly as the wetting angle θ decreases, especially when the angle is around 90°.[28] For graphene with θ = 85°, the water/graphene interface is very weak. With the applied electric bias, the charges concentrate on the convex surface because of the tip effect. This charge concentration would induce an EDL on the convex surfaces, which attracts polar water molecules to form a water bridge on it, significantly enhancing the wettability of the graphene surface. As can be seen in Figure 7B,C, water molecules are aligned in the form of a relatively ordered or icelike structure near the convex surface. This alignment may lead to different properties from bulk water and strengthen the water bridge. As a result, the water bridge may stand longer without the midway collapse during the separation. This ensures more water bridges serving as an adhesive connection between the graphene and SiO_2 substrate. When the electric field is turned off, the water bridge collapses, and consequently the adhesion returns to its normal value.

As shown in Figure 4A, the responding time is different for different RHs. This can be attributed to the water collecting dynamics of the graphene pads. Usually, there is a water layer on the SiO_2 surface in humid air, the thickness of which increases with increasing the humidity.[29,30] In high humidity (e.g., 85%), the water layer could be thick enough for the graphene to form water bridges on the most of the convex regions. Therefore, the adhesive force of the graphene pad immediately reaches its maximum value at high humidity, as shown in Figure 4A. However, for a low humidity (e.g., 58%), the water layer may be too thin to form water bridges at the initial stage of contact. During the contact, the charged graphene pad could continuously collect water from the air or its surroundings. We have directly observed the water generated surrounding a SiO_2 particle when an electric bias is applied on it (Supporting Information, Movie S2). This water may come from the air or existing water layer on the SiO_2 surface. However, it takes time to collect enough water underneath the graphene pad to form water bridges (Figure 8A). Thus, as the number of water bridges changes with time because of the water collection under the bias, the adhesion force changes with time, as observed in the experiment (Figure 4A).

According to the contact splitting principle or size effect,[14] the smaller water bridges can collectively generate much higher adhesive force than a large single bridge. Imagine the replacement of one large spherical water bridge contact of radius R_o by N smaller ones of radius $R = R_o/\sqrt{N}$ with the same total contact area. If the water bridge envelope was known, as schematically shown in Figure 8B, the total adhesive force, F_{ad}, acting on the tip can be calculated as a sum of the capillary force, F_c, tension force, F_t, van der Waals force, F_v, and electric force, F_e

$$F_{ad} = F_c + F_t + F_v + F_e \quad (1)$$

First, the capillary force is caused by the Laplace pressure decrease in the water bridge as a consequence of the negative Kelvin radius, r_K and can be approximately written as[31]

$$F_c = \pi R^2 \gamma_{LV}/|r_K| \quad (2)$$

where γ_{LV} is the interfacial energy of liquid and $r_K = (1/r_1 + 1/r_2)^{-1}$, where r_1 and r_2 are the radii of the water bridge shown in Figure 8B. The tension force is caused by the tension along the triple line, and its z-component can be calculated subsequently[31]

$$F_t = 2\pi\gamma_{LV} R \cos(\theta) \sin(\omega) \quad (3)$$

The van der Waals forces acting between the sphere (diameter D) and the plane was approximated using the equation

$$F_v = HD/(12h^2) \quad (4)$$

where H is the Hamaker constants and h is the characteristic distance ($h \approx 0.2$ nm). Finally, the electrically attractive force can be approximated by

$$F_e = \varepsilon_0 \varepsilon_r \pi R^2 V^2/d^2 \quad (5)$$

where ε_0 and ε_r are the permeability for vacuum and relative dielectric constant, respectively, d is the distance between the electrodes, and V is the applied voltage. Considering the meniscus effect, the adhesion force for simultaneous break of these N bridges is

$$F_{ad} = F_{co} + F_{eo} + \sqrt{N}(F_{to} + F_{vo}) \quad (6)$$

where F_{co}, F_{eo}, F_{to}, and F_{vo} are the capillary, electrical, tension, and van der Waals forces of the large spherical water bridge contact of radius R_o, respectively. According to eq 6, while the capillary and electrical forces remain unchanged, the splitting of a large contact into smaller contacts would lead to an increase in the tension and van der Waals forces by a factor of $\sqrt{N}$. Therefore, increasing the number of nanoconvex contacts−bridges may lead to enhanced adhesion and contribute to adhesion switchability.

Abovementioned four types of forces have different contributions to the overall adhesive force. First, consider the electrically attractive force F_{ao} on the graphene pad (R = 20 μm). According to eq 5 and also considering the effective force on the AFM cantilever, F_{ao} was estimated to be ~0.1 nN for d = 1 mm and V = 10 V, which is negligible. Second, it has been shown that the Hamaker constants for the SiO_2 interfaces in water is much (~5 times) smaller than that in air.[31] The measured adhesive force in dry N_2 is $F_{ad} = F_{vo}$ = 60 nN (Figure 2C). According to eq 4, the van der Waals force of the graphene with the water bridge at high RH should be F_{vo} = 11 nN, which is minimal compared with the measured adhesive force (~350 nN) at high RH. The capillary force F_{co} can be estimated with the Kelvin equation that gives the relationship between the meniscus curvatures r_K and the RH.[32] Because r_K depends on r_1 and r_2 and r_2 could be changed by applying the bias, the capillary force F_{co} would be affected significantly by it. Thus, the bias-induced meniscus could be important in enhancing the adhesion. Finally, the surface tension force is estimated as $F_t \approx 1$ nN for a convex shape with R = 100 nm, and γ_{LV} = 0.0728 N/m, ω = 45° (half surface cover), and θ = 85°, but θ could be reduced by the applied bias because of electric wetting.[33] Considering the enhancement factor of $\sqrt{N}$, the improved wetting will lead to a higher adhesive force. Therefore, the unique topological structures of the graphene surfaces are favorable to the formation of water bridges under applied bias.

Apart from the forces discussed above, the electrostatic interactions between the graphene pad and the microsphere surface could be significant to the switchable adhesion. As shown in Figure 2, there are strong attractive forces before the tip contact the surface during the approaching in humid air under an electrical bias (Figure 2B), and after the tip snaps during the retracting (Figure 2C). This unexpectedly high

DOI: 10.1021/acsami.8b18793
ACS Appl. Mater. Interfaces XXXX, XXX, XXX−XXX

attractive force is caused by the charged graphene pad and water layer on SiO_2 microspheres. As mentioned above, in humid air, there usually are a number of water layers adsorbed on substrates, depending on the RH.[29,30] An EDL is formed through the dissociation of silanol groups: $SiOH \rightarrow SiO^- + H^+$.[30] Under an electric bias, the ions (e.g., H_3O^+ and OH^- ions) may also be generated and polarized with the charges distributed on the surface of the water layer. These surface charges will interact with the tip, resulting in a strong attractive force when the tip approaches to the charged water surface or retreating from it. Because the charges on the graphene pad and SiO_2 microsphere are all generated under the same bias, a formula similar to eq 5 can be derived for the electrostatic force

$$F_e = F_0 \varepsilon_0 \varepsilon_r A V^2 / r^2 \quad (7)$$

where F_0 is the parameter related to geometric and dielectric properties, A is the area of the graphene pad, and r is the distance between the pad and the surface. According to eq 7, the force is proportional to the square of the tip-surface distance and the applied voltage, which is consistent with the experimental results (Figure 2).

From the above analysis, it can be concluded that there is an attractive electrostatic force between the tip and the surface even before the contact. In other words, the nanoconvex surfaces without water bridges would also generate attractive force. As a result, all the convex surfaces of the graphene pad with or without water bridges can generate adhesive forces, which collectively make the adhesion strong and highly switchable.

It should be noted that the conventional electric wetting is operated under a high bias (50−200 V)[34−36] or on very thin insulated films (0−300 nm)[37−39] and can only be used to manipulate the water drops. Here, the nanotextured graphene surfaces can generate a large switchable adhesion and are able to manipulate various micro-/nanosolid objects on a thick silica surface (∼1 mm) under a low bias (∼10 V). This extraordinary capability originates from the unique geometry and conductivity as well as the nonuniform electric field generated by the nanotextured graphene tip. Unlike the conventional electric wetting that has a thin insulated film, the charges on the conductive graphene surface directly interact with water molecules, changing graphene/water bonding that helps modify the overall adhesion at the interface. In addition, under this nonuniform electric field, the polar molecules (e.g., water) will be exerted an electrical force and move toward the graphene surface.[40] With an increase of voltage, the enhanced nonuniform electric field on convex graphene gathers water from humid air or the surrounding surface. Thus, the graphene interface acts as water vapor collecting surfaces, enhancing the switchable adhesion.

It has been shown that electric frequency strongly affects electrowetting. Higher frequency reduces electrowetting.[41] At a low frequency, the ac bias acts like dc bias to enhance adhesion. At a high frequency, water has not enough time to respond to ac bias, and the effective field decreases significantly, leading to a low adhesion similar to that with no bias.

For insulative pads such as LDPE and Teflon, a low bias (∼10 V) is not enough to generate high density of surface charge or surface energy at the pad/water interface, and therefore, no strong EDL is induced by the bias at the interface. Even though LDPE thin films have good wetting ability, bias-induced EDL is not built at the LDPE/water interface. As a result, although the adhesion of LDPE pads increases with increasing the RH, it is insensitive to the bias and exhibits poor switchability. In contrast, N-doped graphene is conductive, hydrophobic, and flexible with the concave−convex surface. The high conductivity facilitates bias-induced EDL or electrowetting at a very low electric bias; the concave−convex structures amplify the bias-induced adhesion for picking up, while hydrophobicity reduces the adhesion for dropping off in micromanipulation. Thus, an effective material design strategy for switchable adhesion would be to enhance conductivity, increase hydrophobicity, and introduce nanoconvex structures on materials surfaces.

4. CONCLUSIONS

We have achieved highly switchable adhesion on the N-doped graphene surfaces. Among the tested Al, Teflon, and LDPE thin films, the N-doped graphene stands out as the best adhesion switchable surface that alters its adhesion dramatically by a factor of ∼6. This graphene surface can pick up, transport, and drop down various microparticles and microfibers for precise patterning without grabbing the objects by force, which reduces the risk of damage. The switchable adhesion and manipulation capability are attributed to its good conductivity, excellent flexibility, unique convex surface nanostructures, and water collecting ability from the air and surrounding surface. The applied bias induces the EDL and icelike structures at the graphene surface, which strengthens the water bridges and consequently enhances switchability of the adhesive force. We envision that this fundamental understanding and materials design strategy can be applied to a wide range of applications such as sticky self-cleaning tapes, climbing robots, nanomanipulators, sensors, drug-delivery, protein separation, to name a few.

5. METHODS

5.1. Preparing Micropads on Tipless AFM Probes. Tipless AFM probes with a length of 225 μm and spring constants ranging 1.1−2.1 N/m (FORTA-TL, AppNano) were selected as manipulator fingers. N-doped graphene, Teflon (PTFE tape, Harvey Inc.), LDPE thin films (ClingWrap, Glad Inc.), and aluminum foils (Reynolds Inc.) were compressed and cut into small pads with a suitable size (∼30 × 30 μm) under the microscope. At the end of cantilevers, epoxy glue (30 min Slow-Cure Epoxy, Kite Studio Co., Inc.) was used to adhere the pads. Probes were then installed to an atomic force microscope (Dimension-Icon AFM, Bruker Co., Inc.). Individual cables were connected to the probe holder and the sample holder, which were connected to a wave generator, as schematically shown in Figure 1A.

5.2. Preparing Microspheres Bonded on SiO_2 Slides and Adhesive Force Measurement. Microspheres chemically bonded on SiO_2 slides were prepared for adhesion measurement under electric bias. SiO_2 microspheres (C-SIO-10.0 Microsphere-Nanosphere Inc.) with a diameter of about 10 μm were cleaned in DI water with an ultrasonic cleaner for 15 min at room temperature. Glass slides (Fisherbrand & Fisherfinest, Fisher Scientific Co., Inc.), the N-type Si wafer, and the gold-coated substrate (Bruker Co., Inc.) were cleaned with DI water, ethanol (459844, Sigma-Aldrich, Co.), and acetone (179124, Sigma-Aldrich, Co.) sequentially and then dried for 24 h in room temperature. Epoxy glue was dispersed first onto a glass slide, and a number of SiO_2 microspheres (∼10 μm) were picked randomly by a micromanipulator (MP-285, Sutter Instrument) and glued on the glass slide one by one. Three sets of SiO_2-microsphere glued slides were prepared for the adhesion measurement.

The measurement of adhesive force of a pad on the glued SiO_2 microspheres was carried out with AFM. In the close loop mode, the

DOI: 10.1021/acsami.8b18793
ACS Appl. Mater. Interfaces XXXX, XXX, XXX−XXX

cantilever with the pad was manipulated by following a programmed trail to perform the forward−contact−retract process, in which the forward−retract speed of Z-piezo was 2 μm/s and contact time (surface delay) on the target was 5 s unless detailed. In continuous force tests, the forward−contact−retract cycles were repeated with 5 s intervals; after the first cycle is completed, 10 V bias was applied on tip-substrate and maintained for 1−2 min until the adhesive force was stable; then, the cycle was kept repeating for one more minute after power off. For each set of parameters, force measurement was tried on 16 randomly selected microspheres, and an average was calculated. RH in the AFM chamber was controlled by filling pure N_2, dry air, and steam or using a dehumidifier in the customized chamber. Potential was applied with a wave generator (33500B, Agilent & MHS-5200P, MH Instek).

5.3. Manipulation of Microparticles on Glass Slides. SiO_2 microparticles with a diameter of 10 μm (C-SIO-10.0, Microsphere-Nanosphere Inc.) were used as the fouling agents. These particles were cleaned using the same procedure as described above and then applied onto a clean glass slide and dried at room temperature for 24 h. Then, the dried particles were transferred to another clean glass slide by tapping the dirtied glass slide over the new slide to form a randomly distributed single particle layer, mimicking a naturally dusted area. The manipulation of the SiO_2 microspheres was carried out with AFM by following the same forward−contact−retract procedure of the force measurement. Pick-up/drop-off tests were performed on 30 microspheres under certain humidity and electric bias. The probability of the particles was calculated to be the number of success tests divided by the total number of tests.

5.4. Molecular Modeling of Graphene Adhesion. The models for adhesion consist of a single graphene convex layer, SiO_2 substrate saturated with silanol groups and water molecules between them. The lateral size of the substrate plates is 50−200 Å, with a thickness of 15−20 Å. The height of the model is kept large (~100 Å), and a number of water molecules are placed in the gap of the substrate and graphene. It is well known that the field inside the conductor is zero, and the excess charges are all on the surface. The charges produce an electric field outside the conductor. For the conductive graphene, charges will distribute on the surface when bias is applied. To simulate the electric field effect, positive (or negative) electric charges equivalent to the applied electric bias are distributed uniformly on the graphene convex. The parameters for water, graphene, and the SiO_2 substrate interactions are described in details as follows:

The total potential of the system is the sum of the bonded interactions and nonbonded interactions

$$V_{\text{total}} = V_{\text{bonded}} + V_{\text{non-bonded}} \tag{8}$$

where the bonded interactions for SiO_2 and graphene are described by the Tersoff potential[42] and modified AIRBO potential,[43] respectively. For silanol groups on the surface of SiO_2, the bonded energies include contributions from bonds and angles of Si−O−H, where Si−O and O−H bonds are described by the Tersoff potential and the three-site models (TIP3P) model for water,[44] and the angle term of Si−O−H is calculated by

$$V_{\text{angle}} = \frac{k_a}{2}(\theta - \theta_0)^2 \tag{9}$$

where k_a is the parameter for angles and θ_0 is the angle at the equilibrium state. Here k_a = 2.51 eV/rad^{-2} and θ_0 = 109.47° are chosen for Si−O−H groups.[45] The nonbonded interactions are taken as the sum of van der Waals (Lennard-Jones) and electrostatic point charge potentials centered on the atoms

$$V_{\text{non-bonded}} = \sum_{i}^{N-1}\sum_{j>i}^{N}\left\{4\varepsilon_{ij}\left[\left(\frac{\sigma_{ij}}{r_{ij}}\right)^{12} - \left(\frac{\sigma_{ij}}{r_{ij}}\right)^{6}\right] + \frac{q_i q_j}{4\pi\varepsilon_0 r_{ij}}\right\} \tag{10}$$

Point charges q_i and q_j located on the atomic nuclei i and j on different molecules are used to model electrostatic intermolecular interactions. Water molecules are modeled by the three-site models (TIP3P) model.[44] The Lennard-Jones parameters for carbon, oxygen, hydrogen, and silicon are listed in Table 2.[46,47] Lennard-Jones potential parameters between unlike atom-type force centers i and j are calculated with the Lorentz−Bertholet combination rules, $\varepsilon_{ij} = (\varepsilon_{ii}\varepsilon_{jj})^{1/2}$ and $\sigma_{ij} = (\sigma_{ii} + \sigma_{jj})/2$.

Table 2. Atomic Charges and Lennard-Jones Interaction Parameters for TIP3P Water, Carbon, and SiO_2 Used in the MD Simulation[44,46,47]

atom	q (e)	σ (Å)	ε (meV)
C		3.468	2.86
O	−0.830 (in OH)−1.0 (Si−O on surface)	3.1507	6.5945
H	0.415 (in OH)	2.98	3.1
Si	1.5 (in Si−O−H)	3.385	25.38

The long-range interactions were computed using the particle−particle particle−mesh algorithm in reciprocal space. Periodic boundary conditions were imposed in x and y directions. MD simulations were performed using LAMMPS with a time step of 0.5 fs for the velocity-Verlet integrator.[22] The system was equilibrated at 300 K for 1 ns, and then, the graphene convex was pulled by applying a displacement of 1.0 Å/ns to it in the z-direction while fixing the bottom of the lower plate. All runs were in the *NVT* ensemble with the temperature controlled by a Nose−Hoover thermostat with a 100 fs damping parameter.

■ ASSOCIATED CONTENT

Supporting Information

The Supporting Information is available free of charge on the ACS Publications website at DOI: 10.1021/acsami.8b18793.

Movie S1 Manipulation processes (AVI)
Movie S2 Water collection of particles (AVI)

■ AUTHOR INFORMATION

Corresponding Author

*E-mail: Zhenhai.xia@unt.edu.

ORCID

Yiyang Wan: 0000-0002-8152-2892
Zhenhai Xia: 0000-0002-0881-2906

Author Contributions

§Y.W. and Y.G. contributed equally to this work.

Notes

The authors declare no competing financial interest.

■ ACKNOWLEDGMENTS

We thank the support from the National Science Foundation under the contract (1266319, 1266295, 1226688). Computational resources were provided by UNT high-performance computing initiative.

■ REFERENCES

(1) Yu, X.; Cheng, H.; Zhang, M.; Zhao, Y.; Qu, L.; Shi, G. Graphene-based smart materials. *Nat. Rev. Mater.* **2017**, *2*, 17046.

(2) Bhullar, S. K.; Lala, N. L.; Ramkrishna, S. Smart Biomaterials-A Review. *Adv. Mater. Sci.* **2015**, *40*, 303−314.

(3) Larson, C.; Peele, B.; Li, S.; Robinson, S.; Totaro, M.; Beccai, L.; Mazzolai, B.; Shepherd, R. Highly Stretchable Electroluminescent Skin for Optical Signaling And Tactile Sensing. *Science* **2016**, *351*, 1071−1074.

(4) Cui, W.; Li, J.; Decher, G. Self-Assembled Smart Nanocarriers for Targeted Drug Delivery. *Adv. Mater.* **2015**, *28*, 1302−1311.

(5) de Crevoisier, G.; Fabre, P.; Corpart, J.-M.; Leibler, L. Switchable Tackiness and Wettability of A Liquid Crystalline Polymer. *Science* **1999**, *285*, 1246−1249.

DOI: 10.1021/acsami.8b18793
ACS Appl. Mater. Interfaces XXXX, XXX, XXX−XXX

(6) Schmidt, S.; Zeiser, M.; Hellweg, T.; Duschl, C.; Fery, A.; Möhwald, H. Adhesion and Mechanical Properties of PNIPAM Microgel Films and Their Potential Use as Switchable Cell Culture Substrates. *Adv. Funct. Mater.* **2010**, *20*, 3235−3243.
(7) Heinzmann, C.; Coulibaly, S.; Roulin, A.; Fiore, G. L.; Weder, C. Light-induced Bonding and Debonding with Supramolecular Adhesives. *ACS Appl. Mater. Interfaces* **2014**, *6*, 4713−4719.
(8) Cheng, Q.; Li, M.; Yang, F.; Liu, M.; Li, L.; Wang, S.; Jiang, L. An Underwater pH-Responsive Superoleophobic Surface with Reversibly Switchable Oil-adhesion. *Soft Matter* **2012**, *8*, 6740−6743.
(9) Zhou, F.; Huck, W. T. S. Surface grafted polymer brushes as ideal building blocks for "smart" surfaces. *Phys. Chem. Chem. Phys.* **2006**, *8*, 3815−3823.
(10) Cheng, Z.; Feng, L.; Jiang, L. Tunable Adhesive Superhydrophobic Surfaces for Superparamagnetic Microdroplets. *Adv. Funct. Mater.* **2008**, *18*, 3219−3225.
(11) Jeong, H. E.; Kwak, M. K.; Suh, K. Y. Stretchable, Adhesion-tunable dry Adhesive by Surface Wrinkling. *Langmuir* **2010**, *26*, 2223−2226.
(12) Tang, C. S.; Dusseiller, M.; Makohliso, S.; Heuschkel, M.; Sharma, S.; Keller, B.; Vörös, J. Dynamic, Electronically Switchable Surfaces for Membrane Protein Microarrays. *Anal. Chem.* **2006**, *78*, 711−717.
(13) Xiao, K.; Zhou, Y.; Kong, X.-Y.; Xie, G.; Li, P.; Zhang, Z.; Wen, L.; Jiang, L. Electrostatic-Charge- and Electric-Field-Induced Smart Gating for Water Transportation. *ACS Nano* **2016**, *10*, 9703−9709.
(14) Xia, Z. H. *Biomimetic Principles and Design of Advanced Engineering Materials*; Wiley: New York, 2016.
(15) Eisner, T.; Aneshansley, D. J. Defense by Foot Adhesion in A Beetle (Hemisphaerota cyanea). *Proc. Natl. Acad. Sci. U.S.A.* **2000**, *97*, 6568−6573.
(16) Xu, Q.; Wan, Y.; Hu, T. S.; Liu, T. X.; Tao, D.; Niewiarowski, P. H.; Tian, Y.; Liu, Y.; Dai, L.; Yang, Y.; Xia, Z. Robust Self-Cleaning And Micromanipulation Capabilities of Gecko Spatulae And Their Bio-Mimics. *Nat. Commun.* **2015**, *6*, 8949.
(17) Qu, L.; Dai, L.; Stone, M.; Xia, Z.; Wang, Z. L. Carbon Nanotube Arrays with Strong Shear Binding-On and Easy Normal Lifting-Off. *Science* **2008**, *322*, 238−242.
(18) Vogel, M. J.; Steen, P. H. Capillarity-based Switchable Adhesion. *Proc. Natl. Acad. Sci. U.S.A.* **2010**, *107*, 3377−3381.
(19) Qu, L.; Liu, Y.; Baek, J.-B.; Dai, L. Nitrogen-Doped Graphene As Efficient Metal-Free Electrocatalyst for Oxygen Reduction in Fuel Cells. *ACS Nano* **2010**, *4*, 1321−1326.
(20) Koenig, S. P.; Boddeti, N. G.; Dunn, M. L.; Bunch, J. S. Ultrastrong Adhesion of Graphene Membranes. *Nat. Nanotechnol.* **2011**, *6*, 543−546.
(21) Gómez-Monivas, S.; Sáenz, J. J.; Calleja, M.; García, R. Field-Induced Formation of Nanometer-Sized Water Bridges. *Phys. Rev. Lett.* **2003**, *91*, 056101.
(22) Cramer, T.; Zerbetto, F.; García, R. Molecular Mechanism of Water Bridge Buildup: Field-Induced Formation of Nanoscale Menisci. *Langmuir* **2008**, *24*, 6116−6120.
(23) Raj, R.; Maroo, S. C.; Wang, E. N. Wettability of Graphene. *Nano Lett.* **2013**, *13*, 1509−1515.
(24) Iler, R. K. *The Chemistry of Silica*; Wiley: New York, 1979.
(25) Verdaguer, A.; Weis, C.; Oncins, G.; Ketteler, G.; Bluhm, H.; Salmeron, M. Growth and Structure of Water on SiO2Films on Si Investigated by Kelvin Probe Microscopy and in Situ X-ray Spectroscopies. *Langmuir* **2007**, *23*, 9699−9703.
(26) Plimpton, S. Fast Parallel Algorithms for Short-Range Molecular Dynamics. *J. Comp. Physiol.* **1995**, *117*, 1−19.
(27) Wei, Z.; Zhao, Y.-P. Growth of Liquid Bridge in AFM. *J. Phys. D: Appl. Phys.* **2007**, *40*, 4368−4375.
(28) Samuel, B.; Zhao, H.; Law, K.-Y. Study of Wetting and Adhesion Interactions between Water and Various Polymer and Superhydrophobic Surfaces. *J. Phys. Chem. C* **2011**, *115*, 14852−14861.
(29) Verdaguer, A.; Weis, C.; Oncins, G.; Ketteler, G.; Bluhm, H.; Salmeron, M. Growth and Structure of Water on SiO2Films on Si Investigated by Kelvin Probe Microscopy and in Situ X-ray Spectroscopies. *Langmuir* **2007**, *23*, 9699−9703.
(30) Iler, R. K. *The Chemistry of Silica*; Wiley: New York, 1979.
(31) Bartošík, M.; Kormoš, L.; Flajšman, L.; Kalousek, R.; Mach, J.; Lišková, Z.; Nezval, D.; Švarc, V.; Šamořil, T.; Šikola, T. Nanometer-Sized Water Bridge And Pull-Off Force In Afm At Different Relative Humidities: Reproducibility Measurement and Model Based on Surface Tension Change. *J. Phys. Chem. B* **2017**, *121*, 610−619.
(32) Matsuoka, H.; Fukui, S.; Kato, T. Nanomeniscus Forces In Undersaturated Vapors: Observable Limit Of Macroscopic Characteristics. *Langmuir* **2002**, *18*, 6796−6801.
(33) Tan, X.; Zhou, Z.; Cheng, M. M.-C. Electrowetting on Dielectric Experiments Using Graphene. *Nanotechnology* **2012**, *23*, 375501.
(34) Cho, S. K.; Moon, H.; Kim, C.-J. Creating, Transporting, Cutting, and Merging Liquid Droplets by Electrowetting-Based Actuation for Digital Microfluidic Circuits. *J. Microelectromech. Syst.* **2003**, *12*, 70−80.
(35) Seyrat, E.; Hayes, R. A. Amorphous Fluoropolymers as Insulators for Reversible Low-Voltage Electrowetting. *J. Appl. Phys.* **2001**, *90*, 1383−1386.
(36) Pollack, M. G.; Fair, R. B.; Shenderov, A. D. Electrowetting-Based Actuation of Liquid Droplets for Microfluidic Applications. *Appl. Phys. Lett.* **2000**, *77*, 1725−1726.
(37) Lomax, D. J.; Kant, P.; Williams, A. T.; Patten, H. V.; Zou, Y.; Juel, A.; Dryfe, R. A. W. Ultra-Low Voltage Electrowetting Using Graphite Surfaces. *Soft Matter* **2016**, *12*, 8798−8804.
(38) Dhindsa, M.; Kuiper, S.; Heikenfeld, J. Reliable and Low-Voltage Electrowetting on Thin Parylene Films. *Thin Solid Films* **2011**, *519*, 3346−3351.
(39) Li, Y.; Parkes, W.; Haworth, L. I.; Ross, A.; Stevenson, J.; Walton, A. J. Room-Temperature Fabrication of Anodic Tantalum Pentoxide for Low-Voltage Electrowetting On Dielectric (EWOD). *J. Microelectromech. Syst.* **2008**, *17*, 1481−1488.
(40) Vemulapalli, G. K.; Kukolich, S. G. Why Does A Stream of Water Deflect in An Electric Field? *J. Chem. Educ.* **1996**, *73*, 887.
(41) Jones, T. B.; Wang, K.-L.; Yao, D.-J. Frequency-dependent electromechanics of aqueous liquids: Electrowetting and dielectrophoresis. *Langmuir* **2004**, *20*, 2813−2818.
(42) Munetoh, S.; Motooka, T.; Moriguchi, K.; Shintani, A. Interatomic potential for Si-O systems using Tersoff parameterization. *Comput. Mater. Sci.* **2007**, *39*, 334−339.
(43) Koelling, D. D.; Harmon, B. N. A Technique for Relativistic Spin-Polarised Calculations. *J. Phys. C: Solid State Phys.* **1977**, *10*, 3107.
(44) Jorgensen, W. L.; Chandrasekhar, J.; Madura, J. D.; Impey, R. W.; Klein, M. L. Comparison of simple potential functions for simulating liquid water. *J. Chem. Phys.* **1983**, *79*, 926−935.
(45) Kroutil, O.; Chval, Z.; Skelton, A. A.; Předota, M. Computer Simulations of Quartz (101)-Water Interface over a Range of pH Values. *J. Phys. Chem. C* **2015**, *119*, 9274−9286.
(46) Pałucha, S.; Gburski, Z.; Biesiada, J. A Molecular Dynamics Study of Fullerene−Carbon Monoxide Mixture. *J. Mol. Struct.* **2004**, *704*, 269−273.
(47) Bruce, P. G.; Freunberger, S. A.; Hardwick, L. J.; Tarascon, J.-M. Li-O2 and Li-S batteries with high energy storage. *Nat. Mater.* **2012**, *11*, 19−29.

DOI: 10.1021/acsami.8b18793
ACS Appl. Mater. Interfaces XXXX, XXX, XXX−XXX